The K2 Galactic Caps Project – going beyond the *Kepler* field and ageing the Galactic disc

B. M. Rendle [1,2]★ A. Miglio [1,2] C. Chiappini,[3] M. Valentini,[3] G. R. Davies,[1,2]
B. Mosser,[4] Y. Elsworth,[1,2] R. A. García,[5,6] S. Mathur,[7,8,9] P. Jofré,[10] C. C. Worley,[11]
L. Casagrande [12] L. Girardi,[13] M. N. Lund [1,2] D. K. Feuillet,[14] A. Gavel,[15]
L. Magrini [16] S. Khan,[1,2] T. S. Rodrigues,[13] J. A. Johnson,[17,18] K. Cunha,[19,20]
R. L. Lane,[21,22] C. Nitschelm[23] and W. J. Chaplin[1,2]

Affiliations are listed at the end of the paper

ABSTRACT

Analyses of data from spectroscopic and astrometric surveys have led to conflicting results concerning the vertical characteristics of the Milky Way. Ages are often used to provide clarity, but typical uncertainties of >40 per cent from photometry restrict the validity of the inferences made. Using the *Kepler* APOKASC sample for context, we explore the global population trends of two K2 campaign fields (3 and 6), which extend further vertically out of the Galactic plane than APOKASC. We analyse the properties of red giant stars utilizing three asteroseismic data analysis methods to cross-check and validate detections. The Bayesian inference tool PARAM is used to determine the stellar masses, radii, and ages. Evidence of a pronounced red giant branch bump and an $[\alpha/\text{Fe}]$ dependence on the position of the red clump is observed from the K2 fields radius distribution. Two peaks in the age distribution centred at ~ 5 and ~ 12 Gyr are found using a sample with $\sigma_{\text{age}} < 35$ per cent. In comparison with *Kepler*, we find the older peak to be more prominent for K2. This age bimodality is also observed based on a chemical selection of low-$[\alpha/\text{Fe}]$ (≤ 0.1) and high-$[\alpha/\text{Fe}]$ (>0.1) stars. As a function of vertical distance from the Galactic mid-plane ($|Z|$), the age distribution shows a transition from a young to old stellar population with increasing $|Z|$ for the K2 fields. Further coverage of campaign targets with high-resolution spectroscopy is required to increase the yield of precise ages achievable with asteroseismology.

Key words: asteroseismology – stars: late type – Galaxy: stellar content, structure.

1 INTRODUCTION

Understanding and classifying the fundamental properties and formation mechanisms of galaxies is a cornerstone of character-izing the evolutionary processes of both galactic and large-scale extragalactic structures. Galactic archaeology is a rapidly expanding field, using fossil remnants within the Milky Way to understand its formation history. The objective of the field is to understand the mechanisms of formation and structure of our Galaxy through the study of the collective properties of stellar populations. Accessing and correctly interpreting this information are key when wanting to understand Galactic evolution, especially during its earliest phases. High-redshift disc galaxies appear to undergo the most significant formation changes between 12 and 8 Gyr ago at $z \approx 2$ (e.g. Madau & Dickinson 2014). The expected bulge, halo, and disc structures are

typically formed during this time, with only thin disc formation steadily continuing to the present. This has been predicted by multiple theoretical models (e.g. Jones & Wyse 1983; Steinmetz & Mueller 1994; Noguchi 1998; Abadi et al. 2003; Sommer-Larsen, Götz & Portinari 2003; Brook et al. 2004; Bournaud, Elmegreen & Martig 2009; Gibson et al. 2009; Bird et al. 2013; Guedes, Mayer, Carollo & Madau 2013; Kawata & Chiappini 2016) and also appears to be true for the Milky Way (Chiappini, Matteucci & Gratton 1997; Chiappini 2009; Minchev, Chiappini & Martig 2013, 2014; Kubryk, Prantzos & Athanassoula 2015; Snaith et al. 2015). Current studies imply that the formation of the thick disc in the Milky Way started at $z \sim 3.5$ (12 Gyr), whilst thin disc formation began at $z \sim 1.5$ (8 Gyr) (e.g. Bensby, Feltzing & Oey 2014; Bergemann et al. 2014; Fuhrmann 2011; Haywood et al. 2013; Robin, Reylé, Fliri, Czekaj, Robert & Martins 2014; Helmi et al. 2018).

There are many unanswered questions in the formation of the Milky Way (e.g. see Minchev 2016; Miglio et al. 2017, for a review).

★ E-mail: bm.rendle8@gmail.com

One of the most fundamental questions is the characterisation of its vertical structure. It is commonly agreed that our Galaxy consists of a central bar/bulge, disc, and halo components (e.g. Bland-Hawthorn & Gerhard 2016; Barbuy, Chiappini & Gerhard 2018). The specific nature of each component has been subject to scrutiny, with the nature of the disc most fervently debated (see e.g. Kawata & Chiappini 2016). Since the results showing evidence for a multiple disc-like structure (Gilmore & Reid 1983), astronomers have striven to fully classify these components and distinguish them chemically, dynamically, and geometrically (see e.g. Freeman & Bland-Hawthorn 2002; Bovy, Rix & Hogg 2012a; Bovy et al. 2012c; Haywood et al. 2013; Rix & Bovy 2013; Anders et al. 2014; Bensby 2014; Recio-Blanco et al. 2014; Hayden et al. 2015; Minchev et al. 2015; Bovy et al. 2016b; Hayden et al. 2017). Typical constraints from the literature define the discs as such: thin disc – scale height $\sim$300 pc, age $\lesssim$ 9 Gyr, solar-[Fe/H], solar-[α/Fe]; thick disc – scale height $\sim$900 pc, age $\gtrsim$ 10 Gyr, [Fe/H] $\sim$−0.7, enhanced [α/Fe] ($>$0.2). Large-scale spectroscopic and kinematic surveys have allowed the dissection of mono-age and mono-abundance populations (e.g. Bovy et al. 2012b, 2016b; Martig et al. 2016; Mackereth et al. 2017; Mackereth et al. 2019), giving snapshots into different epochs of the Milky Way's past. Most studies concur on the existence of multiple stellar populations within the Galactic disc, but stress the importance of which metric is used to define the so-called thin- and thick-disc components, respectively (Bovy et al. 2012a,c; Minchev et al. 2015), if the disc is to be classified as such.

Any inferences to be made about Galactic structure and evolution rely heavily upon having accurate measurements of the stellar population parameters (e.g. ages, metallicities). The relevance of asteroseismology in stellar population studies was recognised early on when the first data from *CoRoT* and *Kepler* became available (see e.g. Miglio et al. 2009; Chaplin et al. 2011a). Subsequently, tests of the precision and accuracy of the asteroseismically inferred parameters enabled quantitative studies that made use of distributions of stellar masses and wide age bins (Miglio et al. 2013; Casagrande et al. 2014; Anders et al. 2017).

This field has continued to mature alongside data-analysis and modelling procedures. It is now recognised that asteroseismic constraints coupled with high-resolution spectroscopy enable inferences on stellar masses, radii, and ages with uncertainties of $\sim$3–10, $\sim$1–5, and $\sim$20–40 per cent, respectively (see Davies & Miglio 2016; Mosser et al. 2019, where seismic yields from different observations are discussed). These uncertainties (in particular in age; see Soderblom 2010, for a comprehensive review of determination methods) are not yet regularly achievable with spectroscopy alone, thus presenting asteroseismology as an attractive prospect for making precise parameter determinations on a large scale.

The upper limits of the asteroseismic age uncertainties are typically achievable using the masses obtained from the so-called asteroseismic scaling relations (Kjeldsen & Bedding 1995). Stellar mass is a particularly valuable constraint in the case of giants, since for these stars age is primarily a function of mass. The age of low-mass red giant stars is largely determined by the time spent on the main sequence, hence by the initial mass of the red giant's progenitor ($\tau_{MS} \propto M/L(M) \propto M_{ini}^{-(\nu-1)}$, with $\nu = 3$–5, e.g. see Kippenhahn, Weigert & Weiss 2012). Though only approximated relations, the masses derived usually translate into more precise ages than those achievable using photometric values and isochrone fitting.
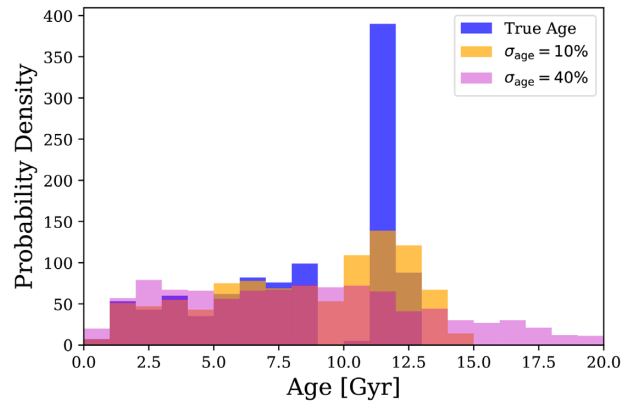

Figure 1. The normalised age distribution for a synthetic MW population (TRILEGAL) is shown (blue). This population is perturbed by age uncertainties of 10 per cent (orange) and 40 per cent (green) to demonstrate the necessity for high-precision age determinations. It is clear that even at 10 per cent some structural details of the population are blurred, with all structure lost when the uncertainty is 40 per cent.

A 30–35 per cent uncertainty in age is sufficient to pull out basic features of a distribution, but is not enough to conclusively interpret the true nature of the underlying population distribution. Fig. 1 illustrates this, showing the effect of different uncertainties on the appearance of the population distribution. Crucially, further accuracy can be achieved when one goes beyond the scaling relations, using asteroseismic grid modelling (inclusion of global asteroseismic parameters in modelling process, e.g. PARAM, Da Silva et al. 2006; Rodrigues et al. 2014, 2017; BASTA, Silva Aguirre et al. 2015) or where possible, the individual acoustic modes themselves (see e.g. Rendle et al. 2019, and references therein). When these techniques are implemented, it is possible to achieve the lower bounds of precision quoted. This precision greatly reduces any ambiguity surrounding the mass, radius, and age distributions, allowing confidence to be given to statements regarding the state of the Milky Way at given epochs.

Though powerful in its capabilities, asteroseismology has been relatively limited to observations of the Galactic mid-plane. *CoRoT* (Baglin et al. 2006; Anders et al. 2017) observed regions in the Galactic inner and outer discs and *Kepler* (Borucki et al. 2010) provided exquisite data for a single field extending out of the Galactic plane. Neither mission, however, sampled sufficient fields for mapping radially and vertically the Milky Way. K2 (Howell et al. 2014) has revolutionised this, with $\sim$80 d observations in the ecliptic plane sampling a broad range of Galactic fields to depths of several kilo-parsecs (kpc). The depth of observations and ability to detect asteroseismic signatures of extensive populations have transformed K2 into an exciting prospect for the provision of improved constraints on Galactic evolution and structure (Stello et al. 2015).

The capability of asteroseismology to determine vertical stellar population trends out to and beyond $\sim$1.5 kpc has already been illustrated with the exquisite data from the *CoRoT* (Miglio et al. 2013) and *Kepler* (Casagrande et al. 2016; Mathur et al. 2016; Silva Aguirre et al. 2018) missions. Re-purposed as K2, asteroseismic observations towards the Galactic poles extend substantively beyond 1.5 kpc, facilitating the first detailed examination of the vertical Galactic structure with asteroseismology. Though degraded

in comparison to *Kepler*, the K2 data remains of high enough quality to make precise asteroseismic inferences (see Chaplin et al. 2015; Stello et al. 2015; Miglio et al. 2016). Hence, using K2 campaigns 3 and 6, we present an asteroseismic analysis of the vertical disc structure of the Milky Way with the K2 galactic caps project (K2 GCP). We demonstrate the increased capability of these campaign fields compared to *Kepler* in determining vertical population trends and show the benefits of improved precision in age.

The paper is laid out as follows. Section 2 describes the K2 campaign fields and used with the different sources of asteroseismic, spectroscopic, and photometric data. Comparisons between data sources are made and effects of the selection function explored. Section 3 briefly details the grid modelling tool used. Sections 4–6 display the key results of the work, based on the analysis of the distributions in radius, mass, and age, of the red giants observed in the two fields C3 and C6 observed by K2. Finally, Section 7 summarizes our findings and discusses the potential of future work.

2 DATA

The K2 mission provided photometric data for a range of fields located both in and out of the Galactic plane for a total of 4 yr, observing 20 campaign fields (C0-19). A dedicated programme for Galactic archaeology has been implemented, with observations of asteroseismic candidates in Galactic regions never previously explored with this technique on this scale. Stello et al. (2015) presents the asteroseismic results for K2 campaign 1, highlighting the potential of the mission and its capabilities. Of the 20 campaign fields, 9 focus on the northern and southern Galactic caps. Asteroseismic analysis of these campaign fields will improve the characterisation of the stellar populations in these directions, which in turn will assist in improving our understanding of the vertical structure.

The K2 Galactic Archaeology Project (K2 GAP; Stello et al. 2017) focuses on the observations of thousands of red giants in each K2 campaign field for the purpose of performing Galactic archaeology with potential asteroseismic targets. Red giant stars are preferentially selected over dwarfs for the K2 GAP as they are intrinsically more luminous, accommodating observations to greater distances and more detail about the Galactic structure to be probed. They also show greater oscillation amplitudes than dwarfs with frequencies well suited to the main long-cadence mode of K2. This allows for asteroseismic detections to be made for a greater sample of the observed population and consequently a more robust analysis of the population parameters.

K2 campaign fields 3 (centred at: $l = 51.1°$, $b = −52.5°$) and 6 (centred at: $l = 321.3°$, $b = +49.9°$) were selected for this work. Campaign field 3 is a south Galactic cap pointing field, whereas campaign 6 points towards the north Galactic cap. Red giant stars in these fields sample Galactic radii typically in the range 6–8 kpc, pointing towards the Galactic centre, and observe stars up to 4 kpc above and below the plane. The depth and range of these observations make these two campaign fields ideal for studies of the vertical properties of the Milky Way as both the so-called thin- and thick-disc populations are expected to be sufficiently sampled.

The observations of the Galactic poles are not limited to two campaign fields. Campaigns 1, 10, 14, and 17 observed the northern, and campaigns 8, 12, and 19 have observed the southern Galactic cap. Though data are available for these fields, they are not included in this work. We limit ourselves to C3 and C6 to explore the potential
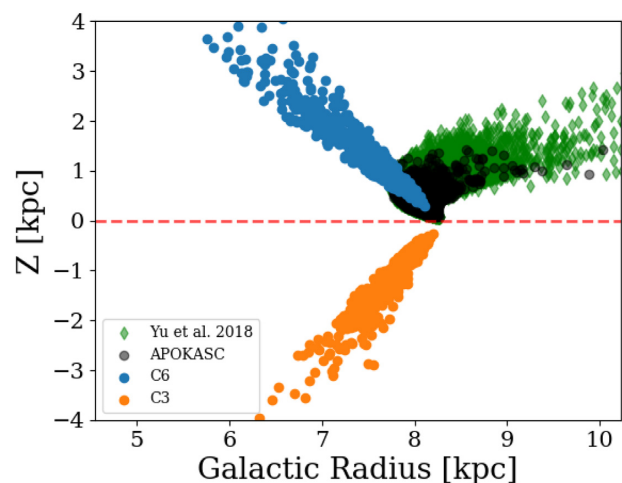

Figure 2. The distribution of stars in the APOKASC (black) and K2 campaigns 3 (orange) and 6 (blue). All Z and R_{Gal} values were calculated using asteroseismic distances. The black cross shows the typical uncertainties in Z and R_{Gal} of the combined K2 sample. The sample of 16 000 red giants from the *Kepler* survey (green diamonds, Yu et al. 2018) shows the full range of the *Kepler* field compared to the APOKASC sample.

of K2 to distinguish trends in the vertical Galactic structure prior to a comprehensive, multicampaign analysis.

For comparative purposes, stars from the nominal *Kepler* mission are included in this work. The stars were selected from the APOKASC catalogue (Pinsonneault et al. 2014, 2017, 2018). Fig. 2 shows the spatial distribution of the APOKASC sample compared to the respective K2 campaign fields used here. The values of Z (vertical distance above the Galactic plane) and R_{Gal} (galacto-centric radius) were determined using asteroseismic distances inferred using the Bayesian inference code PARAM (Rodrigues et al. 2017), with an uncertainty typically below 6 per cent. *Gaia* DR2 (Gaia Collaboration 2018) distances are available for these stars, but the precision of asteroseismic distances has been shown to be approximately a factor of 2 better than current *Gaia* distances for the *Kepler* and K2 C3 and C6 fields (Khan et al. 2019), therefore we adopt the asteroseismic measurements here. However, the *Gaia* parallaxes are used for the determination of stellar radii to investigate the target selection function (see Section 2.2).

The extent to which the K2 fields probe vertically compared to *Kepler* illustrates why this sample is suited for studies of the Galactic structure. It is expected that thick-disc members dominate the stellar population beyond $|Z| \sim 1.5$ kpc, a region poorly sampled by *Kepler* but with significant coverage by K2 across both fields. Increased coverage of stars beyond this distance is crucial for ensuring that a significant thick-disc population is sampled and characterized for definitive conclusions on underlying population trends.

It is also notable from Fig. 2 that the two K2 campaign fields also explore regions in the inner disc, compared to the *Kepler* APOKASC population that is largely restricted to solar Galactocentric radii. Though our study focuses on the vertical properties of the field, the different pointings may be a cause of variability due to differing radial distributions. We take steps to account for this in Section 6.

Multiple subsets of targets are used in this work and for clarity they are named in Table 1. The population name and a brief description of the sample are given for reference. We use a combination of asteroseismic, spectroscopic, and photometric data

Table 1. Population samples used throughout this work. Names and descriptions of the populations are provided.

Sample	Description
K2	K2 sample containing parameters from the K2 EPIC catalogue.
K2 Spec.	K2 cross-matched with spectroscopic surveys. Survey [Fe/H], [α/Fe] (where applicable), and $T_{\rm eff}$ values used.
K2 SM	K2 sample cross-matched with the SkyMapper survey. SkyMapper [Fe/H] and $T_{\rm eff}$ values used.
APOKASC/*Kepler*	PARAM results for the APOKASC-2 population from Miglio et al. (in preparation).
APOKASC α-rich	α-rich APOKASC-2 sample from Miglio et al. (in preparation).
K2 α-rich	K2 Spec. sample with [α/Fe] >0.1.
K2$_{\rm Gaia}$	As K2 SM sample, but with radii calculated from the *Gaia* parallaxes.
K2$_{\rm HQ}$	K2 SM sample; all stars with $\sigma_{\rm age} < 35$ per cent.
K2 Spec.$_{\rm HQ}$	K2 Spec. sample; all stars with $\sigma_{\rm age} < 35$ per cent.

to perform the subsequent analysis. The data used are described in turn below.

2.1 Asteroseismology

Asteroseismic constraints were obtained using three independent asteroseismic analysis methods – BHM (Elsworth et al. in preparation), A2Z (Mathur et al. 2010), and COR (Mosser & Appourchaux 2009). Multiple values for the global asteroseismic parameters $\nu_{\rm max}$ and $\Delta\nu$ were desired to ensure that the final parameters used in the analysis were accurate, allowing for improved inputs for the grid modelling.

The same K2P^2 (Lund et al. 2015) light curves for each K2 campaign were used by each contributor. The same sample of stars was analysed by each method to extract the global asteroseismic parameters: the average large frequency separation ($\Delta\nu$) and the frequency of maximum power ($\nu_{\rm max}$) for each light curve. All of the methods utilize a different method to extract these global parameters. In most cases, multiple methods return a positive detection for the same star. There are also cases where a single method has registered a detection where the others have not.

Having a detection from multiple methods provides an excellent opportunity to explore the consistency of different methodologies and verification of the results. Fig. 3 displays comparisons of $\nu_{\rm max}$ and $\Delta\nu$ values between each of the asteroseismic methods for C3. The distribution of differences between values for crossover stars as a function of the combined uncertainty ($\sigma_{\rm comb.}$, mean uncertainty from cross-matches of all methods summed in quadrature) is shown. The mean (μ) and standard deviation (σ) of each distribution are also included. It is evident that there is greater consistency in $\nu_{\rm max}$ determinations compared to $\Delta\nu$.

The largest disagreements (beyond 2 $\sigma_{\rm comb.}$) typically occur at $\nu_{\rm max}$ around the position of the clump (20–30 µHz), highlighting an area of inconsistency between the different methodologies. Increased discrepancies are expected in this regime though, as the frequency spectra of core helium burning stars show more complex mode patterns and therefore parameter determinations are more dependent on the analysis techniques used.

The $\Delta\nu$ distributions show a larger degree of scatter, as evidenced by their greater standard deviations. The scatter appears consistent across the range of values for each method, with the majority of values within twice the combined uncertainty of each other.

Comparing the distributions to a $N(0,1)$ distribution, it is clear that the standard deviations of the $\Delta(\nu_{\rm max})/\sigma$ distributions are all significantly lower than unity (see Fig. 3). This indicates that the independent analyses show strong agreement, but with a large correlation. The standard deviations of the $\Delta(\Delta\nu)/\sigma$ distributions

are much closer to unity, showing good agreement, but a reduced correlation between methods. These results indicate that there is little disparity in the way $\nu_{\rm max}$ is calculated for these data, but that the methods differ more in how they determine $\Delta\nu$.

2.2 Selection function

The selection function used in this work was adapted from the K2 GAP proposals[1] for C3 and C6 (Sharma et al. in preparation). The K2 GAP selection function was designed to be much simpler to implement than that for the *Kepler* field (Farmer, Kolb & Norton 2013) and to ensure only red giants were observed. Its simplicity affords greater understanding of selection biases, and therefore trends, in the data. Cuts in colour and magnitude ($JHK_{\rm s}$ from the Two Micron All Sky Survey, Skrutskie et al. 2006; V calculated from J and $K_{\rm s}$ as per C6 K2 GAP observing proposal[2]) are implemented within the K2 GAP for campaigns 3 and 6 as follows:

$$\text{C3}: \begin{cases} 9.3 < V < 14.5 \\ J - K_{\rm s} > 0.5 \end{cases} \qquad \text{C6}: \begin{cases} 9 < V < 15 \\ J - K_{\rm s} > 0.5 \end{cases}. \qquad (1)$$

The V-band magnitude cuts differ between fields as the nominal cut for C3 was performed in the H band ($7 < H < 12$). Further, to quantify whether the number of stars with detected oscillations follows the expectations, the asteroseismic detection probability of each star was calculated according to the method described in Schofield et al. (2019) and Chaplin et al. (2011b). In brief, the detection probability test takes an estimate of the seismic $\Delta\nu$ and $\nu_{\rm max}$, the granulation background and a theoretical Gaussian mode envelope for the star centred on the predicted $\nu_{\rm max}$. The signal-to-noise ratio of the estimated total mode power-to-background noise power within the envelope is used to determine the probability of an asteroseismic detection.

The seismic properties mentioned above are estimated using stellar radii and luminosities that were derived using a combination of astrometric and photospheric constraints. Luminosities were inferred from Ks magnitudes, bolometric correction from Casagrande & VandenBerg (2014, 2018a, b, c), extinction calculated using the MWDUST package (Bovy et al. 2016a) with Green et al. (2015) dust maps (extinctions are typically $A_{\rm K} < 0.05$ mag), and distances are based on the *Gaia* DR2 data and the Astraatmadja & Bailer-Jones (2016) method. The input parallaxes were corrected for the zero-point offset based on their field location: -15 ± 4 µas for C3; -2 ± 2 µas for C6 (for calculation, see Khan et al. 2019). The values of $T_{\rm eff}$ used were from the EPIC catalogue.

---

[1] All available at http://www.physics.usyd.edu.au/k2gap/.
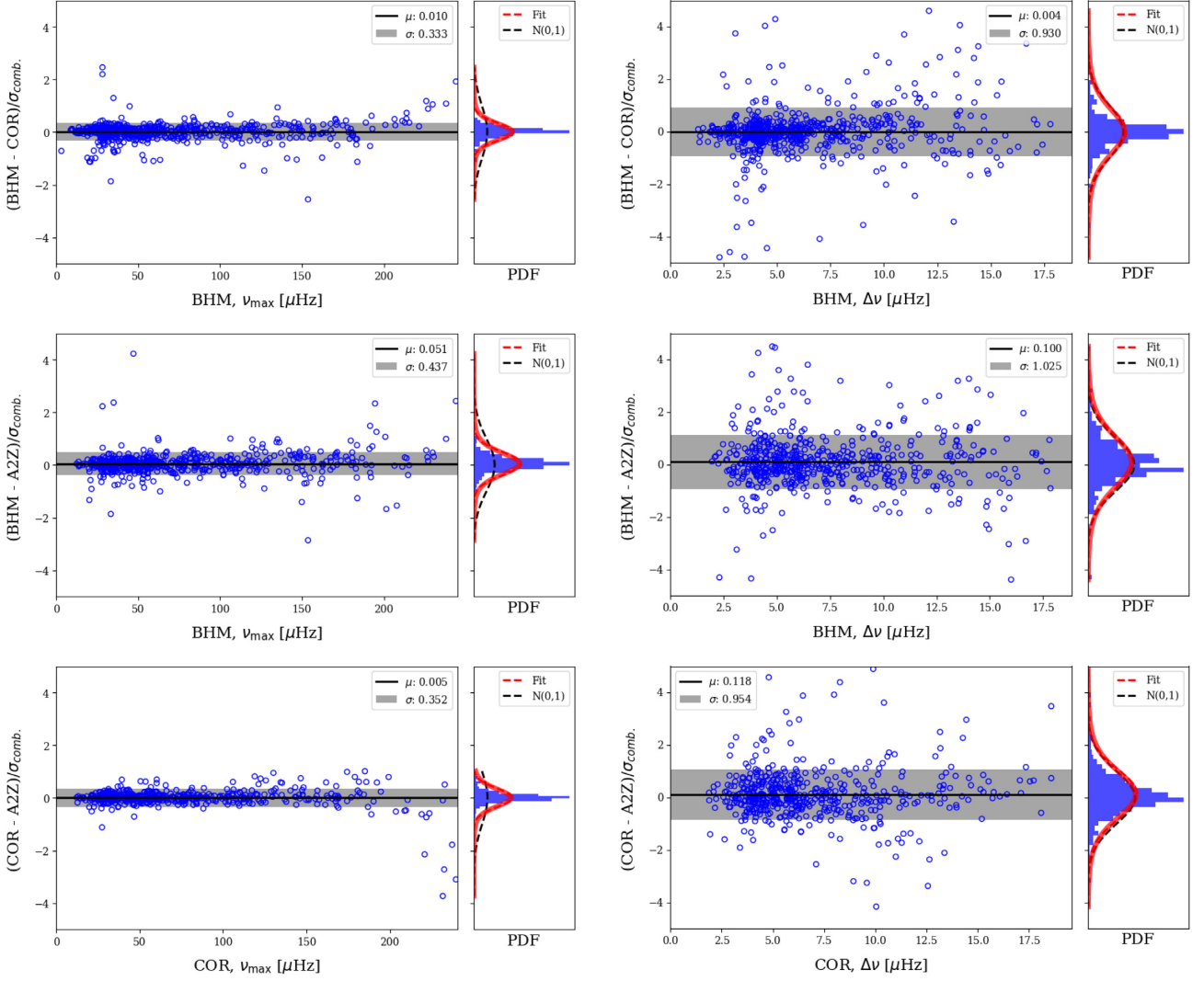[2] See http://www.physics.usyd.edu.au/k2gap/K2/C6 for proposal.

Figure 3. C3 asteroseismic analysis comparisons. *Left:* ν_{max} comparisons. *Right:* $\Delta\nu$ comparisons. *Top:* BHM versus COR. *Middle:* BHM versus A2Z. *Bottom:* COR versus A2Z. The black lines show the mean (μ) and the grey regions the 1σ region of the scatter about the mean. Values are shown in the legend. The histograms show the distribution of points as a function of $N_{\sigma_{comb}}$. The red lines show a Gaussian fit to the data using the values of μ and σ indicated in the legend of the main panel. The black dashed lines show a $N(0,1)$ distribution for comparison.

The colour–magnitude diagram (CMD) in Fig. 4 shows the distribution of all targets in the C3 and C6 fields registered in the K2 GAP target lists. Overlaid is the population of stars passing the detection probability test using radii calculated from the *Gaia* parallaxes. All stars with calculated radii are grouped closely around the beginning of the red giant branch (RGB), the RGB bump (RGBb), and the red clump (RC). This is in line with the expectation of the selection function to remove all MS (main sequence) stars.

The numbers of stars from the K2 GAP predicted to pass the detection probability tests for C3 and C6 were 1073 and 1822, respectively. The numbers of stars with actual detections within the predicted sample were 762 for C3, and 1374 for C6. There is an ~ 25 per cent reduction between the predicted and actual counts. The reductions predominantly affect faint-magnitude ($H > 10$, $V > 12$) stars. In C3, the initial star count with detections from the asteroseismic analysis is 885. Considering stars with both observational values for ν_{max} and $\Delta\nu$, 818 remain after the detection probability cut is made. Uncertainty in the estimate of the asteroseismic parameters for the K2 GAP sample is a possible

source of the discrepancy, as are additional sources of instrumental noise not accounted for in the noise model.

A scaling relation was used to predict ν_{max} for the K2 GAP sample for use in the probability test. Since stellar mass is not known, ν_{max} was estimated from *Gaia* radii, T_{eff} from the EPIC catalogue, and calibrated to the known K2 GAP ν_{max} values from observations. The final form of the relation to estimate ν_{max} was

$$\nu_{max} \propto \left(R T_{eff}^{-0.5} \right)^{-1.86}. \tag{2}$$

The values of R and T_{eff} were varied within typical uncertainties, resulting only in a small (<10 stars) difference between counts in each case. Hence, we consider unlikely that inaccuracies in the predicted ν_{max} are the main source of the discrepancy between the number of expected and returned detections.

The noise model applied in the detection probability test follows that first proposed for *Kepler* in Chaplin et al. (2011b), modified for the noise performance of K2 by Lund et al. (2016). The procedure predicts the expected global signal-to-noise level in the
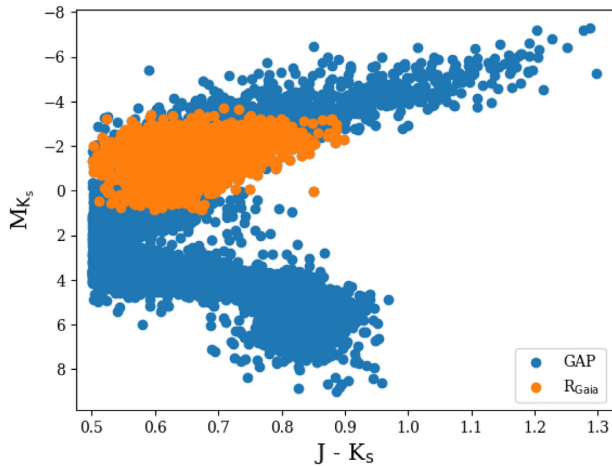
Figure 4. CMD for the C3 and C6 combined K2 GAP target lists. The blue markers indicate the original K2 GAP sample. Orange indicates the stars passing the detection probability test using radii derived from the *Gaia* parallaxes.

Table 2. The number of stars in final samples for each K2 campaign field and supplementary surveys used in this work.

Survey	C3	C6
K2	483	929
K2 SM	377	646
RAVE	85	83
Gaia-ESO	38	–
APOGEE	101	25
K2 Spec.	128	102

detected oscillations against background from intrinsic stellar noise (granulation) and shot/instrumental noise. This approach assumes that the population model is a good model of observations. Though the predictions work well for the majority of stars, in reality some show higher noise than expected (i.e. the tendency is for the distribution of real stars to show a high-noise tail), which could be a potential contributor to the lower actual numbers of detections returned by the different methods (see Mosser et al. 2019, for a review of factors affecting seismic performance).

After the detection probability test, a final cut was implemented based on observational detections. Stars with fewer than two independent detections were removed. Multiple detections were sought to improve the reliability of the measurement by cross-referencing. The values of ν_{max} and $\Delta\nu$ were deemed consistent and the star accepted if the independent values lay within 2σ of another. The final asteroseismic inputs were selected from the COR and BHM methods due to a greater yield of detections and less conservative uncertainties compared to A2Z. Though not explicitly used, the A2Z determinations are consistent with the final asteroseismic inputs.

Table 2 states the final number of stars remaining from each survey after the selection cuts. The values associated with K2 are the final sample sizes after they have been cross-matched with improved photometric metallicities and effective temperatures (see Section 2.3.3).

2.3 Photospheric constraints

2.3.1 Spectroscopy

As with the asteroseismic data, multiple sources of spectroscopic data have been used to increase the yield of stars with such data. Once more, it is necessary to evaluate the consistency of these data to ensure that a set of consistent results can be achieved independent of the spectroscopic survey used.

The spectroscopic data were collected to complement those from asteroseismology, improving upon the values of parameters such as T_{eff} and [Fe/H] that can be obtained from photometry. The data from the RAVE (C3/C6, Kunder et al. 2017), APOGEE (C3/C6, DR16, Eisenstein et al. 2011; Majewski et al. 2017; we make use of data to be released as a part of the Sloan Digital Sky Survey IV, Gunn et al. 2006; Holtzman et al. 2015; Nidever et al. 2015; García Pérez et al. 2016; Blanton et al. 2017; Zasowski et al. 2017), and *Gaia*-ESO (C3, Worley et al. in preparation; Gilmore et al. 2012) surveys have been used. After the selection cuts had been applied, these data were cross-matched with the asteroseismic data. The final number of stars with spectroscopic information is low compared to the total sample (see Table 2), but still remains significant enough to draw sensible conclusions from the data and verify the wider trends observed with the larger photometric sample. Spectroscopic parameters from RAVE and *Gaia*-ESO were calibrated by adopting and iterating with asteroseismic $\log(g)$ values (Valentini et al. 2017; Worley et al. in preparation). Also, the $\log(g)$ values for the APOGEE sample are from asteroseismology, although the metallicities and T_{eff} are derived using the APOGEE spectroscopic $\log(g)$.

Though a thorough comparison between the surveys is beyond the scope of this paper, we bring attention to a source of potential bias within our results. We do not attempt to calibrate between surveys, but only demonstrate some differences between them.

The use of multiple sources of spectroscopic data is excellent for maximising the yield of targets, but comes with its own complexities. There is often little consistency between survey observations, with observations of different spectral domains and resolutions common (Valentini et al. 2016; Jofré, Heiter & Soubiran 2018). In addition, each survey has a set of unique selection biases that need to be considered, which can manifest in systematic parameter trends (e.g. see Anguiano et al. 2018; Jönsson et al. 2018). Cross-calibrating surveys thus proves difficult. Even where overlaps exist, it is not easy to directly compare the values (Jofré, Heiter & Buder 2017).

Comparisons and attempts to calibrate surveys to one another were made for this work in order to have a consistent spectroscopic sample. Fig. 5 shows the comparison between the surveys used in C3, where an overlap of more than 10 stars was available (APOGEE to *Gaia*-ESO; RAVE to *Gaia*-ESO). The relations between T_{eff}, $\log(g)$, and [Fe/H] are described by linear, orthogonal distance regressions (ODRPACK, scipy, Jones et al. 2001), with the resultant fits displayed on the relevant subplots. It is evident that though the uncertainties (APOGEE $\sigma_{Fe/H}$ inflated by a factor of 20) maintain consistency between values in each case, each gradient departs significantly from unity or is systematically offset. This is particularly strong in temperature and [Fe/H], revealing inconsistencies between the surveys. Consistent methodology to calibrate the $\log(g)$ values means reduced scatter, but a departure from unity is still observed.

Considering the scatter between surveys, prior to the modelling process the uncertainties on [Fe/H] and T_{eff} were increased to

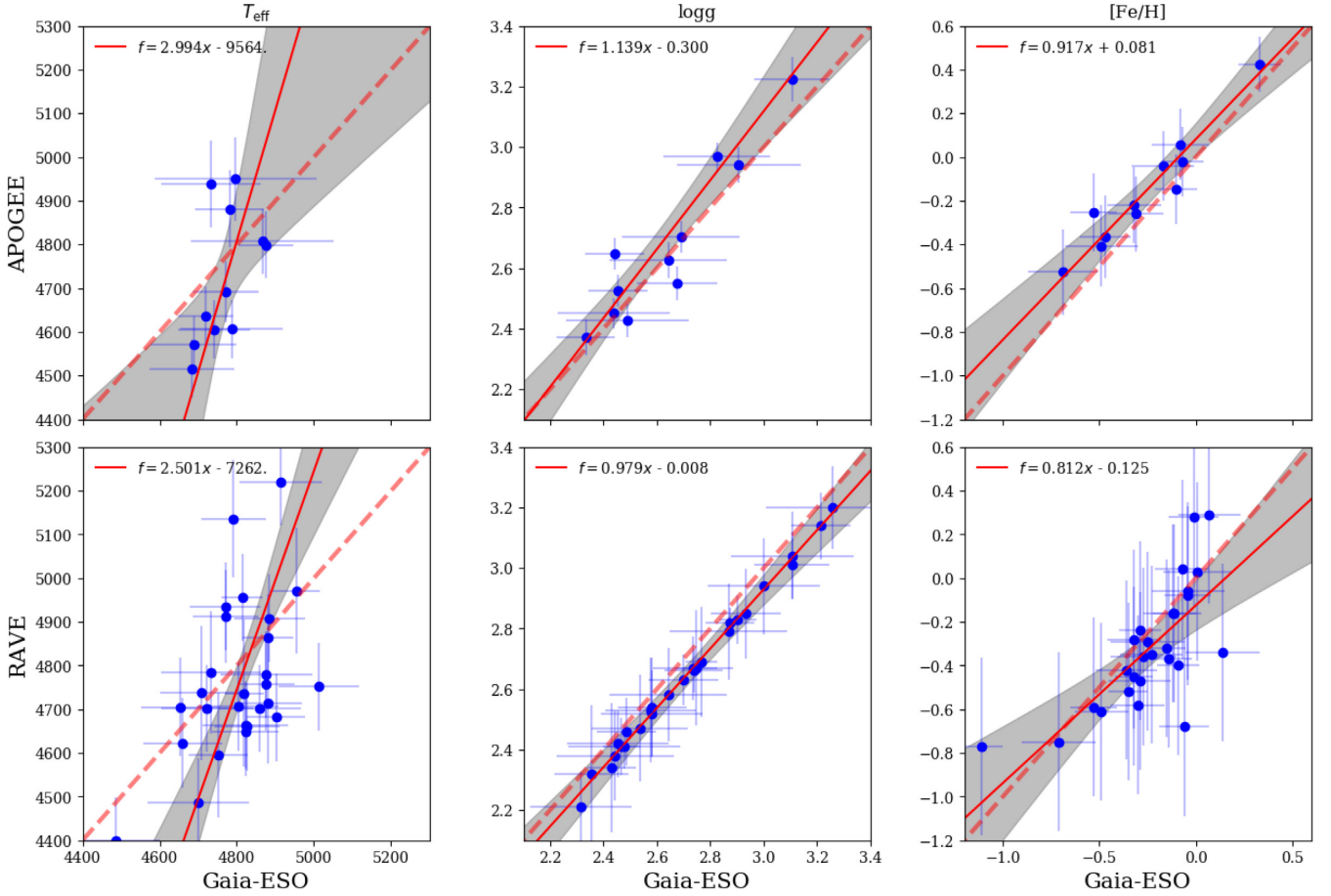**Figure 5.** A comparison between the C3 spectroscopic data sources for $T_{\rm eff}$ (left-hand panels), log(g) (middle), and [Fe/H] (right). Comparisons for APOGEE and *Gaia*-ESO (top row) and RAVE and *Gaia*-ESO (bottom row) are displayed. The blue points represent the data, with associated uncertainties. The red, dashed lines are the one-to-one relation to guide the eye. The red solid line is the best fit (f) to the data (equations given in the legends) and the grey regions denote the confidence intervals of the fits.

account for the observed differences. The variance between surveys was of the order of 50 K in $T_{\rm eff}$ and 0.1 dex in [Fe/H], respectively. These values were adopted as the systematic uncertainty between surveys and were added in quadrature to the initial survey values. The resultant values are conservative uncertainties for the spectroscopic parameters.

2.3.2 Chemical composition

Chemical space is often a key area used in the literature to distinguish between stars belonging to a thin- or thick-disc population. Typically, the thin disc is expected to be [Fe/H] rich and solar-[α/Fe]; the thick disc [Fe/H] poor and [α/Fe] enriched (e.g. see Fuhrmann 1998; Bensby et al. 2005, 2007; Reddy & Lambert 2008; Ruchti et al. 2011; Kordopatis et al. 2015). This trend is a consequence of the expected epochs of formation of these structures. The thick disc is considered to be older (10–12 Gyr) and has therefore formed rapidly in conditions with less metal enrichment and greater α-enhancement from core-collapse supernovae. The thin disc is thought to have started forming later (7–9 Gyr ago) and, as a consequence, is more metal-rich due to enrichment of the interstellar medium by type-Ia supernovae (see e.g. Matteucci 2001, and references therein).
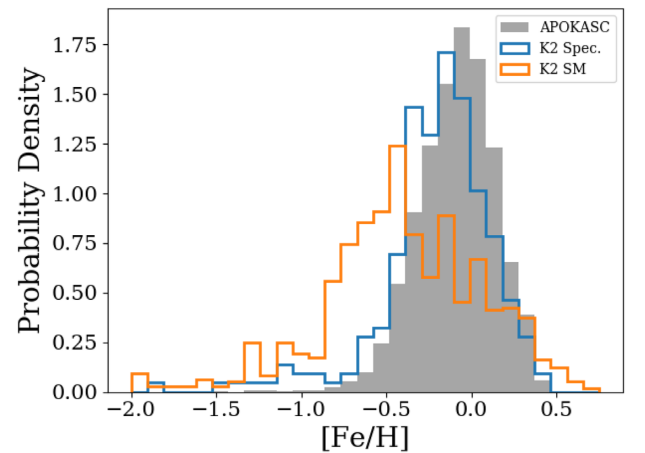

Figure 6. Normalised [Fe/H] distributions for the APOKASC (grey), K2 stars with spectroscopic values (blue), and SkyMapper values (orange).

The metallicity distributions observed with *Kepler* and the K2 fields studied here further demonstrate the suitability of the K2 fields for this study and are shown in Fig. 6. The *Kepler* distribution peaks at [Fe/H] of -0.1 dex with a standard deviation of ±0.5 dex. This
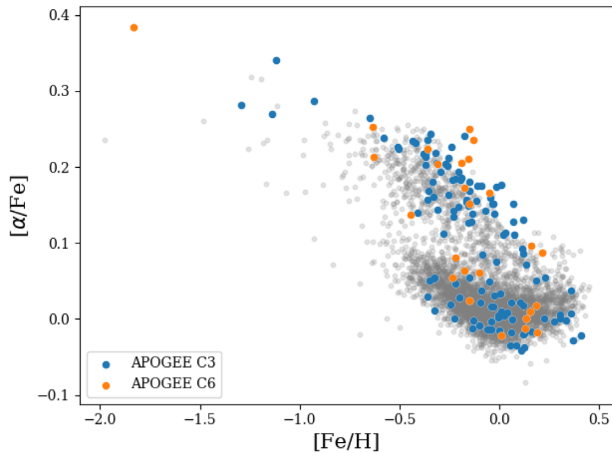
Figure 7. [Fe/H] versus [α/Fe] distribution for the APOGEE survey in the K2 C3/C6 samples. The APOKASC distribution is shown in grey. The cross shows the typical uncertainties in [Fe/H] and [α/Fe] in the sample used.

distribution is highly indicative of a thin-disc-dominated population, with only a small tail in the metal-poor regime. A peak for the thick disc would be expected at around −0.5 dex (see Minchev et al. 2013, 2014, and references therein). The [Fe/H] values have typical uncertainties of 0.21 dex.

The K2 Spec. distribution follows closely that of the APOKASC sample, though it peaks at a lower metallicity (−0.25 dex). The whole sample is clearly shifted towards lower metallicity and has an extended metal-poor tail. Given the greater vertical extension of K2 C3 and C6, the sample is likely to have a dominant contribution from the thick disc, explaining the shift compared to APOKASC. The K2 SM sample alludes to a much greater metal-poor tail than K2 Spec. shows. This is potentially true, but the photometric distribution has greater scatter compared to the RAVE and APOGEE survey metallicities (see Casagrande et al. 2019). This is demonstrated by the extension to unlikely metallicities of >0.5 dex for K2 SM.

The [Fe/H] versus [α/Fe] distribution for the K2 APOGEE and APOKASC samples is shown in Fig. 7. The same spectroscopic survey has been used here for a direct comparison to negate the effect of any biases due to the survey selection function. The typically expected low- and high-α sequences associated with the evolution of the thin and thick discs are evident for these populations. Classifying the α-rich population as in Table 1 ([α/Fe] > 0.1), ∼ 60 per cent of the K2 C3/C6 sample consists of α-rich stars compared to only ∼ 15 per cent of the APOKASC sample. It is thus necessary to include comparisons of the K2 samples to the α-rich component of APOKASC and not only the full sample. Though the proportion of stars in this regime is smaller than in the K2 populations, the sample size is still significant enough (748 stars) for comparisons and conclusions to be drawn.

2.3.3 Photometry

Spectroscopic temperatures and metallicities were not available for all of the stars in the initial sample. To supplement this information, photometric values of T_{eff} and [Fe/H] determined from observations by the SkyMapper survey (Keller et al. 2007; Wolf et al. 2018) have been used. SkyMapper is designed to take *uvgriz* photometry, from which stellar parameters can be derived (Casagrande et al.

2019). The reported survey parameters have been calibrated using GALAH (Buder et al. 2018) spectroscopic metallicities and T_{eff} from the InfraRed Flux Method, and validated against APOGEE DR14 (Abolfathi et al. 2018) and RAVE DR5 to ensure reliable parameter determinations.

The SkyMapper survey has covered most of the southern sky, subsequently observing stars across both C3 and C6. This provides a coherent photometry source for the fields and parameter determinations. Parameters were not available for all of the stars in the two campaigns, but the total number of stars remains significant for understanding population trends (377 – C3; 646 – C6). As they number fewer, the stars with spectroscopic values are considered a subsample of the total photometric population in this work. The spectroscopic values should provide tighter constraints on the final parameter distributions and better information regarding the chemistry of the stars than the photometry considering the higher resolution observations. These are therefore viewed as a benchmark to which the larger photometric sample can be compared and underlying trends identified/ratified.

2.4 Synthetic data

In addition to using the *Kepler* APOKASC data to provide a comparative sample for the K2 data, a synthetic population was also generated using the TRILEGAL (a TRIdimensional modeL of thE GALaxy; Girardi et al. 2012) population-synthesis code. The code allows one to generate a synthetic population of a specific region of the Galaxy, with user-defined Galactic components, initial mass function, and star formation rates. We computed two synthetic populations based on the central coordinates of the C3 and C6 fields and the field of view of the *Kepler* telescope. A uniform star formation rate from 9 Gyr to present was chosen for the thin disc and a 1 Gyr burst at 11 Gyr for the thick disc.

3 METHOD

We use grid-based stellar modelling to extract the fundamental parameters of the stellar ensembles. A grid of models generated using MESA (Modules for Experiments in Stellar Astrophysics; Paxton et al. 2015) in conjunction with the Bayesian inference tool PARAM (Da Silva et al. 2006; Rodrigues et al. 2014, 2017) was used.

From the measured observational constraints (T_{eff}, [Fe/H]), ν_{max}, and $\Delta\nu$), PARAM computes probability distribution functions for the stellar parameters (e.g. radius, mass, age). The code uses a flat prior age and an initial mass function from Chabrier (2001). An upper age prior can also be set, which we set as 20 Gyr. Though greater than the accepted age of the Universe, current uncertainties on stellar ages are typically greater than 30 per cent. Ages up to 20 Gyr are consistent with being drawn from a normal distribution centred on the Hubble age with $\sigma = 30$ per cent.

Parameter values are determined statistically from the output probability density functions (PDFs) produced by PARAM (Rodrigues et al. 2017). A choice of using the median or mode statistic is available to the user. The 68th and 95th percentiles are returned for all parameters in each case.

We adopt the modal values as the preferred choice of final parameter. The modal value is most representative of the distribution peak, particularly when approaching the limits of the underlying grid boundaries and priors. Post-process, stars caught on the prior boundaries of the grid in age are removed from the sample. These stars are forced to specific ages, potentially distorting the final

parameters returned. An upper limit to the prior of 20 Gyr was used. This is reflective of the age distribution observed in Fig. 1, whereby stars with high uncertainty are attributed ages beyond the expected age of the Universe. The final sample sizes of C3 and C6 are 377 and 646, respectively (10 and 6 per cent reduction compared to the values in Table 2).

4 RADII

An examination of the distribution of radii within the K2 sample provides a good indicator if a typical population of red giant stars is observed. Though the distribution will vary between observed populations, key features such as the RC should be obvious from a pronounced peak at $\sim$10–11 $R_\odot$. Fig. 8 displays this characteristic, indicating the clump sample within the data. The figure shows a comparison of PARAM (i.e. asteroseismic) radii for K2 SM and APOKASC (panel A) and PARAM to *Gaia* K2 SM (panel B; $\sigma_\varpi/\varpi < 10$ per cent cut applied) radii. Comparing K2 to APOKASC provides context for the results, but comparing the radii derived using PARAM and those computed using the *Gaia* parallaxes provides insight into which values are most appropriate to use in future analyses. The *Gaia* distribution at the RC peaks at a lower radius than that from PARAM for the same stars. As discussed in Section 2.2, this shows evidence of an underestimation of the stellar radii compared to asteroseismology.

An unexpected secondary peak at $\sim$7–8 $R_\odot$ is present in both the spectroscopic and photometric K2 data. The secondary peak is also a feature of a sample analysed in Miglio et al. (in preparation). The sample is a population of α-rich ([α/Fe] >0.1) stars from the APOKASC catalogue. This α-rich sample shows comparable features to those observed with the K2 stars, indicating that the feature is typically common to an older population, a trait synonymous with α-enhanced stars. A detailed examination of a Kiel diagram (Fig. 9) of the populations shows an overdensity of stars located at the RGB-bump, which is synonymous with the overdensity in radius observed.

Interestingly, there is a slight difference in the peak of the clump distributions of the full and α-rich samples for both APOKASC and K2. The clump distribution for the α-rich APOKASC sample peaks 0.5 $R_\odot$ lower than the full population. More metal-poor stars were found to have lower radii. This difference is less significant ($\sim$0.1 $R_\odot$) in K2. Simulations from TRILEGAL predict that this is also related to the expected Galactic component that a star is a member of. The clump of the thick disc peaks at the observed α-rich radii and the thin disc at the full APOKASC radii as one may expect (see Fig. 8, panel C). The trend is a function of $T_{\rm eff}$, driven by mass and metallicity. Evidence of this can be seen in Fig. 10. Here, a Hertzsprung–Russell diagram, coloured by metallicity, of a K2 C3 TRILEGAL simulation is shown. It is evident that there is a division in the RC population, whereby more metal-poor stars are situated at hotter temperatures, hence, a lower radius than more metal-rich stars, given that the luminosity is very similar. This is highlighted further by the inset of Fig. 10, which shows a zoom in of the RC population. The overlaid evolutionary tracks (as in Fig. 9) show this as a function of mass too. The hot clump sample (>4900 K) lies close to the low mass and metallicity track (0.8 $M_\odot$; -0.5 dex), whereas the cooler clump sample (<4900 K) is positioned closest to the high mass and metallicity track (1 $M_\odot$; -0.25 dex).

A separation in the populations in radius is apparent (though some contamination from first ascent RGB stars is present), further confirming the trends observed in Figs 8 and 10. This is not conclusive evidence that the positioning of the peak clump radius
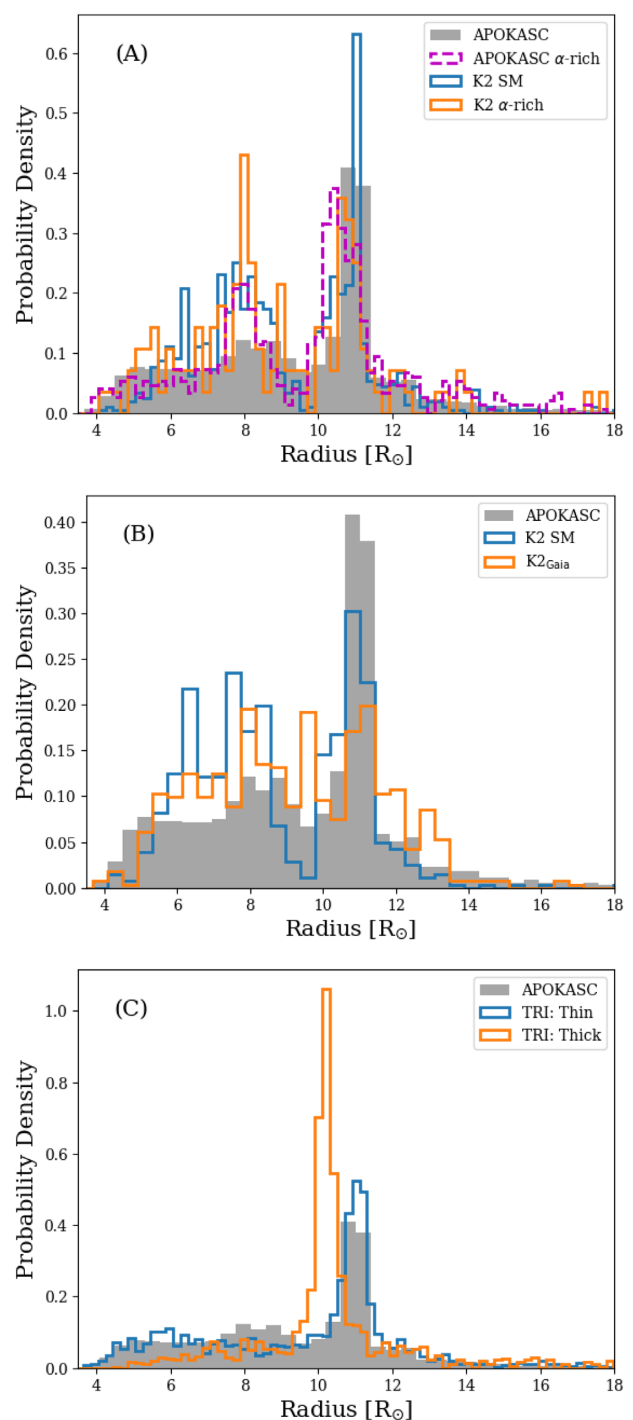

Figure 8. *(A):* Radius distributions from PARAM for the APOKASC (grey), APOKASC α-rich (magenta, dashed), K2 SM (blue), and the K2 α-rich (orange) samples. *(B):* Comparison of *Gaia* (magenta) and seismic (blue, PARAM) radius distributions for the same stars in K2 SM. Only stars with $\sigma_\varpi/\varpi < 10$ per cent are shown. *(C):* TRILEGAL simulation of the K2 C3 field. The thin-disc (blue) and thick-disc (orange) populations within the simulation are shown. All distributions are normalised.
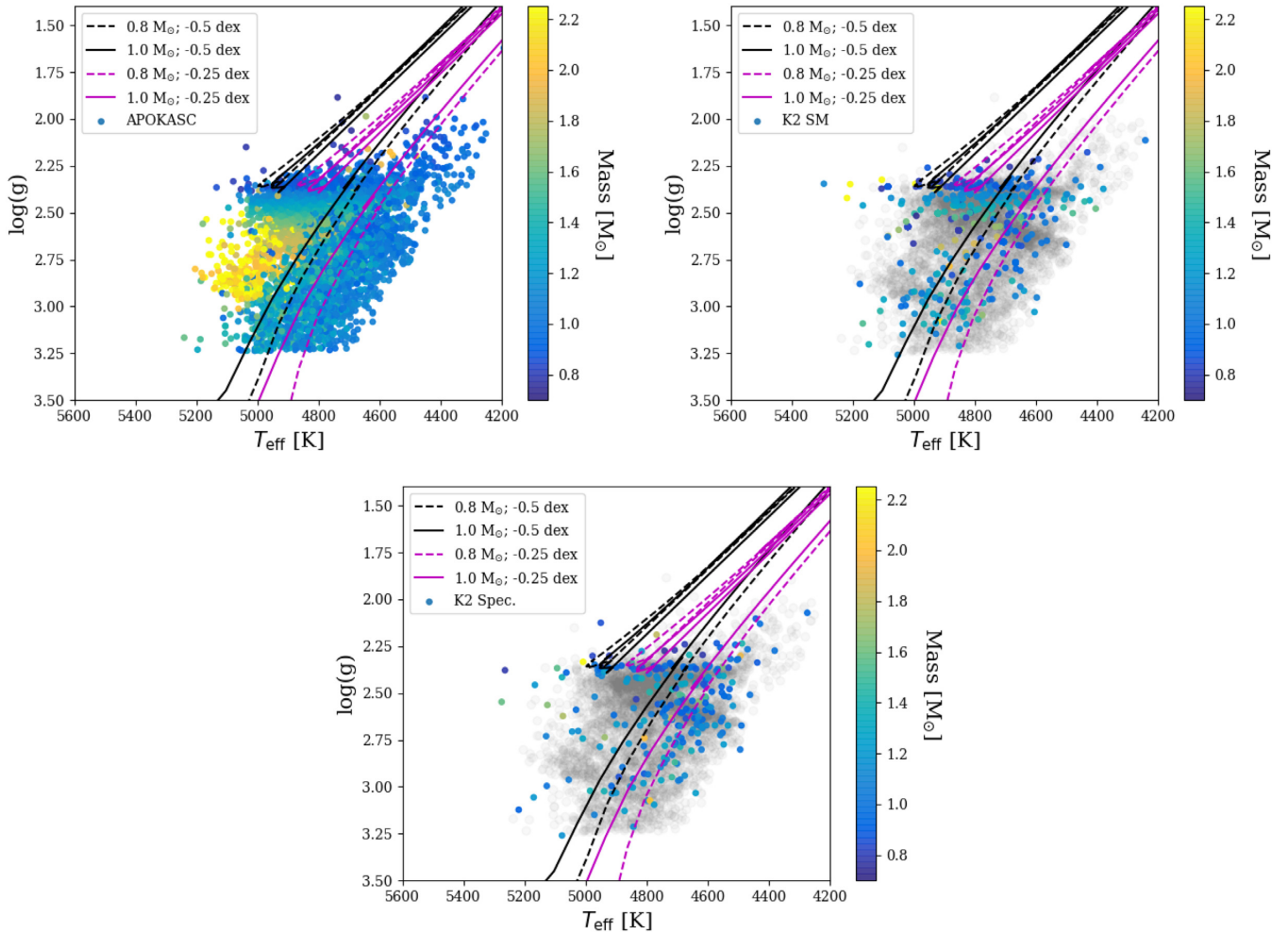
Figure 9. Kiel diagram with mass colour bar for the APOKASC (top left), photometric (top right), and spectroscopic (bottom) K2 samples. Tracks of different mass (0.8 M$_\odot$ – dashed; 1.0 M$_\odot$ – solid) and metallicity (−0.5 dex − black; −0.25 dex − magenta) are overlaid as a guide. The α-rich APOKASC population is included in grey. The grey lines denote the location of the RGB-bump (RGBb).

can be used as a tracer for Galactic components/evolution, but opens up possibilities to explore this further (see Girardi 2016, and references therein).

5 MASSES

Given the tight age–mass relation expected for red giant stars (Kippenhahn & Weigert 1990), stellar masses inferred by aster-oseismology provide an excellent proxy for age (e.g. see Miglio 2012; Davies & Miglio 2016). Understanding the mass distribution of a population therefore allows early inferences about the expected age distribution to be made. Panel A of Fig. 11 shows the mass distribution of the K2 SM, K2 Spec., and APOKASC samples as a function of vertical height, Z, from the Galactic plane. It can be seen that all samples show a trend of increasing vertical extent with decreasing mass. There is evidence of a metallicity gradient, with decreasing metallicity observed as one moves out of the plane and towards lower masses. These trends are comparative with those expected of a thin/thick-disc structure, in particular with the low masses extending to greater vertical extent being reflective of the expectation of observing older stars further from the plane (see Section 6; Miglio et al. 2013; Casagrande et al. 2016).

The remaining panels of Fig. 11 show the resultant populations after additional cuts/reanalyses of the K2 SM and K2 Spec. data were made (same alterations applied to the background APOKASC samples). The effects due to using masses from scaling relations (Kjeldsen & Bedding 1995) (B), removing the RC by radius (C), and using a grid including microscopic diffusion (D) were explored to test for any property dependences within the populations. Except additional scatter at low masses when the scaling relations are used (a likely overestimation of the masses; see e.g. Rodrigues et al. 2017, and references therein) and varying sample sizes, the initial trends seen in panel A are invariant to the changes implemented. The high mass scatter and shape of the mass/Z relations remain consistent throughout, as does the perceived metallicity gradient. The robustness of these trends gives confidence to the derived stellar properties in the K2 SM and K2 Spec. samples being a true reflection of the population and its features.

Fig. 12 shows the mass distributions of both the full and α-rich APOKASC and K2 populations. The distributions show that the K2 SM sample contains a larger proportion of low-mass stars than in APOKASC, suggesting that the population of these K2 fields is potentially older than that of APOKASC and is discussed further in Section 6. It is also shown that the number of α-rich stars in these
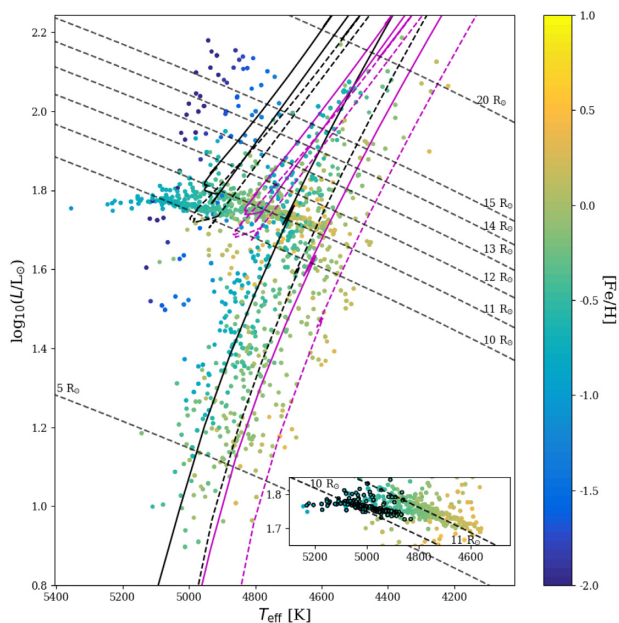
Figure 10. HRD of a K2 C3 TRILEGAL simulation. An [Fe/H] colour bar has been used, with lines of constant radius included (grey dashed line; values marked on plot). Tracks of different mass (0.8 $M_\odot$ – dashed; 1.0 $M_\odot$ – solid) and metallicity (−0.5 dex – black; −0.25 dex – magenta) are overlaid as a guide. *Inset:* An enlargement of the RC population, with stars classified as thick disc in the simulation denoted by black circles. Only RC stars are shown here, using the classifier in TRILEGAL.

populations is enhanced for lower masses, suggesting the older a red giant star is, the more α-enhanced it is likely to be.

6 AGES

Many arguments surrounding the definition of the thin and thick discs, in particular their formation, centre largely on the age distribution of the populations and indications of enhanced star formation. Conclusively proving a distinction in age between the populations defined geometrically and/or chemically is difficult due to typical age uncertainties of > 40 per cent. The samples used in this work have median uncertainties of < 35 per cent (X_{HQ} samples), allowing general trends to be extracted.

Fig. 13 shows a comparison of the age distributions[3] of the APOKASC (Miglio et al., in preparation), $K2_{HQ}$, and K2 Spec.$_{HQ}$ samples for stars with age uncertainties < 35 per cent. Each set of stars was analysed with an extended age prior of 20 Gyr, hence the unphysically extended age ranges. As previously stated, the magnitude of the uncertainties is such that these values remain consistent with the age of the Universe within $1\sigma - 2\sigma$. It is the features of the distributions that are of most interest though. The APOKASC population follows closely the age distribution for giants shown by Casagrande et al. (2016) with a large peak at 5 Gyr and a smaller peak at 11 Gyr. In addition, the α-rich population maps closely the distribution presented in Silva Aguirre et al. (2018). The distribution peaks broadly at $\sim$12 Gyr, with a small overdensity at 3 Gyr due to a population of young α-rich stars (e.g. see Fuhrmann 2011; Chiappini et al. 2015; Martig et al. 2015;

---

[3]Kernel Density Estimates were generated using the PYTHON module PYQT-FIT, 1DKDE. Default smoothing applied.

Jofré et al. 2016; Johnson & APOKASC Collaboration 2016). The dominance of the 12 Gyr peak in the α-rich population indicates that this influences the appearance of the secondary peak in the nominal APOKASC sample. A reduced prominence at 12 Gyr for the α-poor ([α/Fe]<0.1) APOKASC sample confirms this, reaffirming the expectations that older stellar populations have enhanced α-element abundances. The consistency of our results with these studies gives confidence to make clear comparisons with results from K2.

Considering the APOKASC and K2 populations extend vertically beyond 1 kpc, it is expected that some mixing will occur between disc populations as the thin disc transitions up into the thick disc. Hence, both the samples should contain a prominence related to each component. The broadness of the peaks is not of concern here as it is known that the K2 data are not as high quality as the *Kepler* data and therefore greater uncertainties are expected. Fig. 1 shows the impact of different age uncertainties on the shape of a simulated distribution. Large uncertainties mask the original features, emphasising the importance of obtaining high-precision age determinations.

The $K2_{HQ}$ photometric and K2 Spec.$_{HQ}$ distributions are shown in the centre and right-hand panels of Fig. 13. The $K2_{HQ}$ distribution peaks predominately at 5 Gyr in concordance with APOKASC. The distribution then passes through a minimum at $\sim$9 Gyr before gradually increasing again towards older ages. This differs slightly to the spectroscopic sample, which shows an earlier minimum at 8 Gyr (as with APOKASC) and a clearly defined secondary peak at 14 Gyr. Given the current uncertainties on age and the fact that the two samples differ both in magnitude range and in photospheric parameters (e.g. for the stars in common, the spectroscopic temperatures are on average $\sim$50 K lower than SkyMapper's), these small apparent age differences are likely due to be dominated by target selection biases and systematic effects. K2 Spec.$_{HQ}$ also shows a more even weighting between the young and old peaks, suggesting a split population. As previously discussed, the K2 age uncertainties are larger compared to APOKASC, which contributes to the overall washing out and extension of features in the distributions. The greater defined features of the spectroscopic sample compared to the photometric are symptomatic of the quality of the input parameters used in the analysis, with the spectroscopic surveys providing improved input parameters and, hence, final uncertainties. Similarly to with APOKASC, the α-rich and α-poor spectroscopic components from APOGEE were plotted. It is clearly shown that the young and old peaks are dominated by the α-poor and α-rich subsamples, respectively. This further confirms the expected chemical dichotomy of stars from different generations.

The higher age peak, and larger proportion of stars at older ages when using spectroscopic inputs, indicates that the K2 fields contain an older population than the *Kepler* sample; but is this just a radial selection effect or due to sampling a greater vertical extent? Considering the majority of the APOKASC sample extends out to 1 kpc, the population trends for the $K2_{HQ}$ stars above and below ±1 kpc are also shown on the centre panel of Fig. 13. The sample below 1 kpc follows closely that of the APOKASC sample, with a very clearly defined young population at 5 Gyr, but has few stars beyond 10 Gyr, with the distribution dropping off significantly and flattening beyond 9 Gyr. In contrast, the population beyond 1 kpc shows a minimal peak at $\sim$5 Gyr and dominant old population peak at 15 Gyr. The difference in the shape of the age distributions above and below 1 kpc is stark enough to show that the stellar population changes with increasing Z.

For further confirmation that the age distribution changes primarily with Z and not with Galactic radius, Fig. 14 shows the age
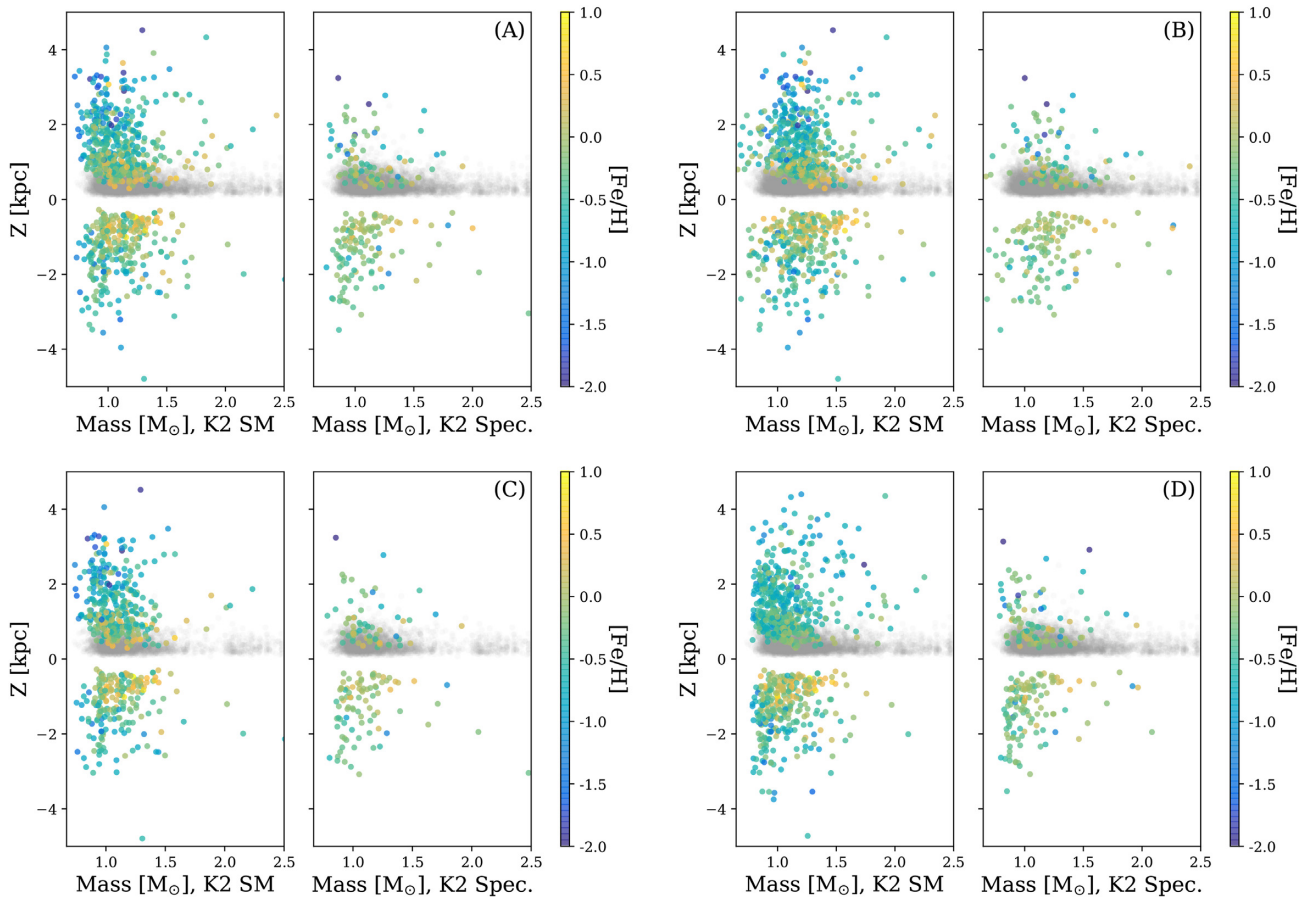
Figure 11. Mass against vertical height above and below the Galactic plane (*Z*) for the K2 SM (left) and K2 Spec. (right) samples in each panel. An [Fe/H] colour bar is shown. The metallicity scale is the same for each subplot. The APOKASC sample is shown in grey. *(A):* Original K2 SM and K2 Spec. samples. *(B):* Masses calculated from scaling relations. *(C):* Red clump population has been removed. *(D):* Populations reanalysed with a grid including diffusion.
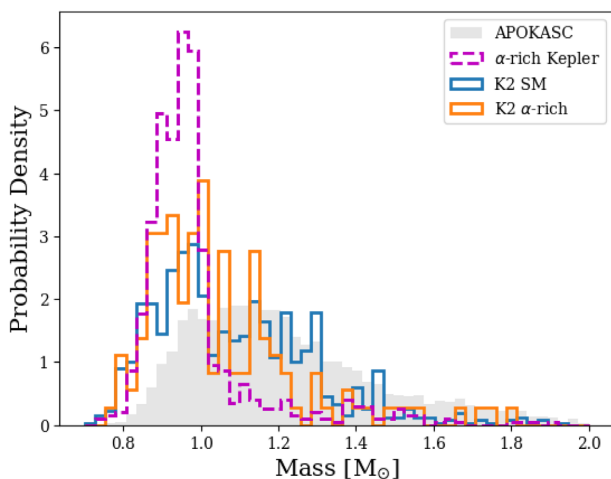

Figure 12. Normalised mass distributions from PARAM for the APOKASC (grey), APOKASC α-rich (magenta, dashed), K2 SM (blue), and the K2 α-rich (orange) samples.

distribution of the $K2_{HQ}$ field and APOKASC samples in vertical bins of 0.5 kpc. The C3 field was chosen as this field samples significantly beyond 1.5 kpc after all cuts are applied, whereas C6 contains too few stars beyond 1.5 kpc for sensible conclusions. For the same reasoning, the APOKASC sample is only shown out to 1.5 kpc. The first two bins of Fig. 14 (0–1 kpc) show that the APOKASC and K2 populations follow each other closely. A two-sample Kolmogorov–Smirnoff test confirms this consistency with *p*-values greater than 0.05 for each bin ($p_{Z < 0.5} = 0.28$, $p_{0.5 < Z < 1.0} = 0.09$), rejecting the hypothesis that the APOKASC and K2 C3 population age distributions are significantly different in these ranges. This is a good indication that, up to 1 kpc, the age distribution of similarly selected stars is expected to be the same at these different Galactic radii. Consequently, any further inferences can be concluded to be due to the vertical rather than radial properties of the fields.

Reflecting the trend observed in Fig. 13, the bins beyond 1 kpc show an increasingly divergent population, with consistent young and old populations. This was not expected due to the typical belief that the thick disc is composed of older stars. An explanation of this is the presence of the aforementioned young (<7 Gyr), α-rich stars. Considering the K2 Spec., $\sigma_{age} < 35$ per cent sample, ∼ 8 per cent of the stars (accounting for increased intrinsic uncertainties on age compared to *Kepler*) fall into this category, compared to ∼ 2 per cent in APOKASC (same σ_{age} cut). Of these stars, 20 per cent can be found beyond 1 kpc from the Galactic mid-plane. This indicates an expectation to see non-insignificant numbers of these stars at high |*Z*|. Fig. 15 illustrates this trend. The figure is a replication of Fig. 2, but only for the K2 Spec.$_{HQ}$ sample and is coloured by age. It is readily apparent that the older population stars (>10 Gyr) dominate at high-|*Z*| (>|1.5| kpc), but contamination by young stars is clearly
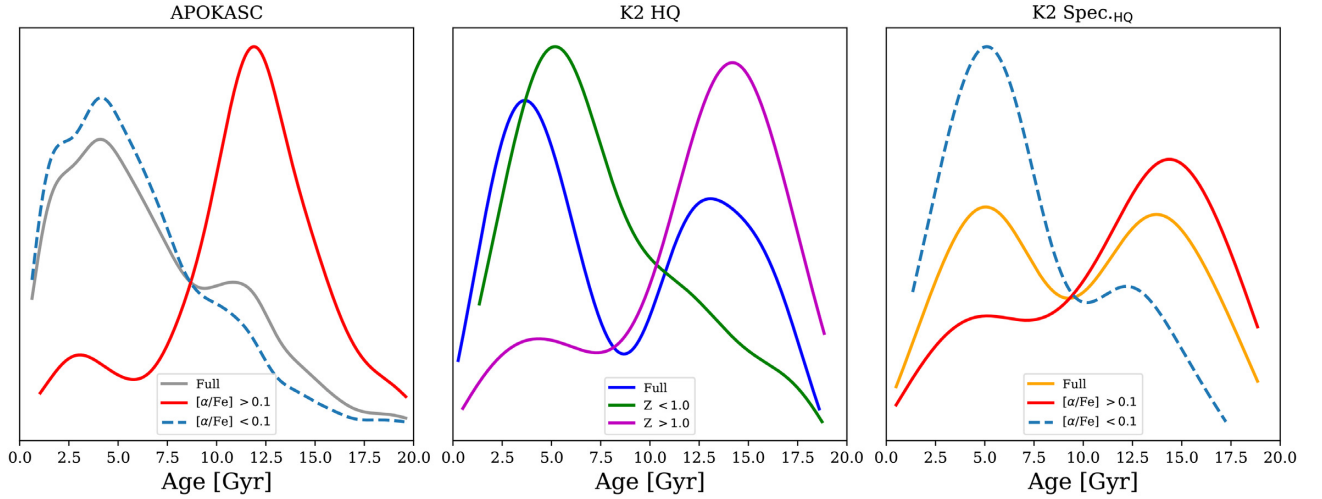
Figure 13. Normalised age distributions for the APOKASC and K2 populations. *Left:* Nominal (grey), α-rich (red), and α-poor ([α/Fe]<0.1; blue dashed) APOKASC sample age distributions. *Middle:* K2$_{HQ}$ complete (blue), $|Z| < 1.0$ kpc (green), and $|Z| > 1.0$ kpc (purple) distributions. *Right:* K2 Spec.$_{HQ}$ (orange) and K2-APOGEE α-rich (red) and α-poor ([α/Fe]<0.1; blue dashed) distributions.
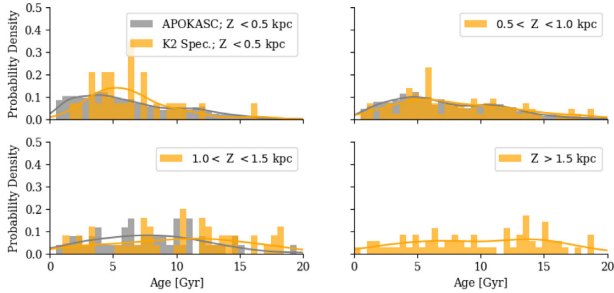

Figure 14. K2 Spec.$_{HQ}$ sample age distribution as a function of Z (0.5 kpc bins). A comparison to the APOKASC sample is performed up to 1.5 kpc as beyond this the numbers are insufficient for a meaningful comparison. Samples of stars with $\sigma_{age} < 35$ per cent are shown.
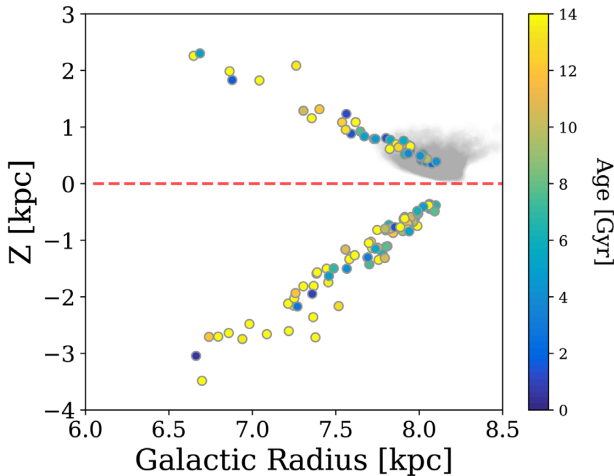
Figure 15. As Fig. 2, but showing the age distribution of the K2 Spec.$_{HQ}$ sample.

visible. This population also begins to demonstrate the bimodality in [α/Fe] between the discs, with some members of the young thick disc showing similar chemical properties to the older population. Only a small number of these stars have been observed, though.

The significance of the population will only be known once a larger sample has been studied. The implications of the findings may be significant for understanding some of the mechanisms of Galactic evolution.

The young, α-rich stars are not the only young stars at high $|Z|$ (e.g. Jofré et al. 2016; Hayes et al. 2018). There are many questions surrounding the young populations far from the Galactic mid-plane. These include whether these stars have formed *in situ*; they migrated and have been captured as they pass through this region of the Milky Way; or are they products of stellar binary evolution and mergers (Izzard et al. 2018)? Each scenario has implications on the evolution of the Galactic structure. A thorough treatment of the kinematics is required to further disentangle the origins of these stars. Though not a pressing concern for this work, future exploration with the *Gaia* data to examine the kinematics and orbits of these stars will be undertaken to determine if they indeed belong to this population or are migrators.

The shape of the age distributions is a reflection of the star formation history of the Galaxy. A feature in common for all of the age distributions shown in Fig. 13 is a minimum. The presence of this feature is indicative of a quenching period, in which the star formation rate drops and reduction in stars of certain ages is observed. With well-defined peaks in both the K2 SM and APOKASC distributions, there is evidence to support two epochs of star formation. Tighter age constraints are required before the lengths of any epochs of suppressed/enhanced star formation can be confirmed, but the results are concurrent with predictions of a cessation in star formation at ~9 Gyr (e.g. Haywood et al. 2016) and the predictions of the two-infall model (Chiappini, Matteucci & Gratton 1997; Chiappini, Matteucci & Romano 2001; Chiappini 2009) of distinct formation epochs for the thin ($|Z| \leq 1.0$ kpc, [α/Fe] ≤0.1, age ~9 Gyr) and thick ($|Z| > 1.0$ kpc, [α/Fe] >0.1, age >10 Gyr) discs.

7 CONCLUSION

K2 campaign fields 3 and 6 have been used to demonstrate further the capacity of K2 as a Galactic archaeology mission. The existence of observations towards the Galactic poles in addition to the *Kepler* field highlights the importance of these observations to contributing

towards some of the key questions surrounding the existence of the Galactic thin and thick discs.

Initial investigations of the K2 campaigns C3 and C6, and *Kepler* populations provided evidence of the K2 fields presented containing a larger proportion of metal-poor stars than found with the *Kepler*. Further differences were found in the sample parameter distributions:

(i) *Radii* – Both populations exhibited the expected prominence due to the RC, but the K2 distribution showed an additional, more pronounced compared to *Kepler*, peak at $\sim 8\,R_\odot$. The feature was also found to be significant in a sample of *Kepler* α-rich stars. It relates to the RGB-bump, and its prominence in three fields of different pointing means that it could be used as a potential indicator of α-rich stellar populations in future.

A shift in the position of the RC peak was observed between the *Kepler* full (APOKASC) and α-rich (APOKASC α-rich) samples. The α-rich sample showed a peak 0.5 $R_\odot$ lower for the clump compared to the full sample. Using a TRILEGAL simulation of the *Kepler* field, a divergence in the clump location was evidenced when using the simulation's Galactic component identifier. The α-rich peak aligned with TRILEGAL expectations of the thick-disc population as it is expected to be older and metal poor. The full sample aligned with the thin disc peak. The position of the peak of the RC could therefore be considered as an indicator of the type of population being observed, but additional research beyond the scope of this paper would be required to establish this.

(ii) *Mass* – We demonstrate the robustness of our results to population variance and underlying physical prescriptions when considering the mass against Z distribution of the K2 fields. A trend of decreasing mass with increasing $|Z|$ is observed, with some scatter at high mass. We also find evidence of a decreasing metallicity gradient with decreasing mass and increasing $|Z|$. These trends remain consistent when different mass sources are used, the RC is removed from the population, and a different underlying grid is used for the analysis. The robust nature of these global trends lends confidence to our inferences of global population properties being representative of the sample.

(iii) *Ages* – As an excellent example of one of the most metal-poor asteroseismic populations observed, the resultant K2 age distributions reveal possible epochs of enhanced star formation. The observed sample also shows the evolution of the age distribution as a function of height above the Galactic mid-plane, matching the *Kepler* sample closely out to ~1 kpc in concordance with the works by Casagrande et al. (2016) and Silva Aguirre et al. (2018), but differing significantly beyond this distance. Further investigation clearly indicated that as Z increases, the population becomes dominated by older stars. The changing distributions not only lend support to the theories indicating that the thick disc is older than the thin disc, but also reaffirm the desire for precise ages to allow for the confirmation of any possible epoch of quiescence in star formation and age bimodality associated with chemistry. It must be noted that some young stars (<4 Gyr; possible binary products or migrators) remain at high Z and require further investigation as to their origin and nature.

A strong bimodality was also observed in the age distribution for both the *Kepler* and the K2 fields (Fig. 13), with distinct young and old population peaks at 5 and 14 Gyr. Clear associations with $|Z|$ and [α/Fe] were attributed to each peak: 5 Gyr – low-α, $|Z| \leq$ 1.0 kpc (thin disc); 14 Gyr – high-α, $|Z| > 1.0$ kpc (thick disc). The chemical age dichotomy was also confirmed with the *Kepler* sample, where the peak at 12 Gyr is due to the α-rich population. Each

sample presented contains a minimum, suggestive of a time delay between the formation of these populations. Given the geometric and chemical characteristics of the old and young populations, the argument can be made that this is representative of a time difference in the formation histories of the thin and thick discs.

Further work remains prior to making definitive conclusions on the true age profile of the Galactic disc. The K2$_{HQ}$ sample shows a glimpse of what is achievable with improved precision in age determination, as does the K2 Spec. sample. However, an increase in the sample size is necessary to lend further weight to our conclusions regarding the population properties. The asteroseismic yield of stars towards the Galactic poles is continuing to increase with all-sky observations from the NASA TESS mission (Ricker et al. 2015) currently in progress.

An increase in spectroscopic coverage of the K2 campaign fields would yield improvements in parameter determination though, with the known high quality of the asteroseismic inferences linked closely to the quality of input spectroscopic parameters. With more wide-field spectroscopic surveys coming online in the near future (e.g. WEAVE, 4MOST), in addition to increased asteroseismic information from additional K2 campaign fields with observations of the Galactic poles, the field is well positioned to continue to exploit the opportunities afforded by the K2 mission to understand the true nature of the vertical structures of the Milky Way.

REFERENCES

Abadi M. G., Navarro J. F., Steinmetz M., Eke V. R., 2003, ApJ, 591, 499
Abolfathi B. et al., 2018, ApJS, 235, 42
Anders F. et al., 2014, A&A, 564, A115
Anders F. et al., 2017, A&A, 597, A30
Anguiano B. et al., 2018, A&A, 620, A76
Astraatmadja T. L., Bailer-Jones C. A. L., 2016, ApJ, 832, 137
Baglin A., Auvergne M., Barge P., Deleuil M., Catala C., Michel E., Weiss W., COROT Team, 2006, in Fridlund M., Baglin A., Lochard J., Conroy L., eds, ESA SP-1306: The CoRoT Mission Pre-Launch Status - Stellar Seismology and Planet Finding. ESA, Noordwijk, p. 33
Barbuy B., Chiappini C., Gerhard O., 2018, ARA&A, 56, 223
Bensby T., 2014, in Feltzing S., Zhao G., Walton N. A., Whitelock P., eds, Proc. IAU Symp. 298, Setting the Scene for Gaia and LAMOST. Kluwer, Dordrecht, p. 17
Bensby T., Feltzing S., Lundström I., Ilyin I., 2005, A&A, 433, 185
Bensby T., Zenn A. R., Oey M. S., Feltzing S., 2007, ApJ, 663, L13
Bensby T., Feltzing S., Oey M. S., 2014, A&A, 562, A71
Bergemann M. et al., 2014, A&A, 565, A89
Bird J. C., Kazantzidis S., Weinberg D. H., Guedes J., Callegari S., Mayer L., Madau P., 2013, ApJ, 773, 43
Bland-Hawthorn J., Gerhard O., 2016, ARA&A, 54, 529
Blanton M. R. et al., 2017, AJ, 154, 28
Borucki W. J. et al., 2010, Science, 327, 977
Bournaud F., Elmegreen B. G., Martig M., 2009, ApJ, 707, L1
Bovy J., Rix H.-W., Hogg D. W., 2012a, ApJ, 751, 131
Bovy J., Rix H.-W., Liu C., Hogg D. W., Beers T. C., Lee Y. S., 2012b, ApJ, 753, 148
Bovy J., Rix H.-W., Hogg D. W., Beers T. C., Lee Y. S., Zhang L., 2012c, ApJ, 755, 115
Bovy J., Rix H.-W., Green G. M., Schlafly E. F., Finkbeiner D. P., 2016a, ApJ, 818, 130
Bovy J., Rix H.-W., Schlafly E. F., Nidever D. L., Holtzman J. A., Shetrone M., Beers T. C., 2016b, ApJ, 823, 30
Brook C. B., Kawata D., Gibson B. K., Freeman K. C., 2004, ApJ, 612, 894
Buder S. et al., 2018, MNRAS, 478, 4513
Casagrande L., VandenBerg D. A., 2014, MNRAS, 444, 392
Casagrande L., VandenBerg D. A., 2018a, 599 BCcodes: Bolometric Corrections and Synthetic Stellar Photometry. Astrophysics Source Code Library, record ascl:1805.022
Casagrande L., VandenBerg D. A., 2018b, MNRAS, 475, 5023
Casagrande L., VandenBerg D. A., 2018c, MNRAS, 479, L102
Casagrande L. et al., 2014, ApJ, 787, 110
Casagrande L. et al., 2016, MNRAS, 455, 987
Casagrande L., Wolf C., Mackey A. D., Nordlander T., Yong D., Bessell M., 2019, MNRAS, 482, 2770
Chabrier G., 2001, ApJ, 554, 1274
Chaplin W. J. et al., 2011a, Science, 332, 213
Chaplin W. J. et al., 2011b, ApJ, 732, 54
Chaplin W. J. et al., 2015, PASP, 127, 1038
Chiappini C., 2009, in Andersen J., Nordström B., Bland-Hawthorn J., eds, Proc. IAU Symp. 254, The Galaxy Disk in Cosmological Context. Kluwer, Dordrecht, p. 191
Chiappini C., Matteucci F., Gratton R., 1997, ApJ, 477, 765
Chiappini C., Matteucci F., Romano D., 2001, ApJ, 554, 1044
Chiappini C. et al., 2015, A&A, 576, L12
Da Silva L. et al., 2006, A&A, 458, 609
Davies G. R., Miglio A., 2016, Astron. Nachr., 337, 774
Eisenstein D. J. et al., 2011, AJ, 142, 72
Farmer R., Kolb U., Norton A. J., 2013, MNRAS, 433, 1133
Freeman K., Bland-Hawthorn J., 2002, ARA&A, 40, 487
Fuhrmann K., 1998, A&A, 338, 161
Fuhrmann K., 2011, MNRAS, 414, 2893
Gaia Collaboration, 2018, A&A, 616, A1
García Pérez A. E. et al., 2016, AJ, 151, 144
Gibson B. K., Courty S., Sánchez-Blázquez P., Teyssier R., House E. L., Brook C. B., Kawata D., 2009, in Andersen J., Nordström B., Bland-Hawthorn J., eds, Proc. IAU Symp. 254, The Galaxy Disk in Cosmological Context. Kluwer, Dordrecht, p. 445
Gilmore G., Reid N., 1983, MNRAS, 202, 1025
Gilmore G. et al., 2012, The Messenger, 147, 25
Girardi L., 2016, ARA&A, 54, 95
Girardi L. et al., 2012, in Miglio A., Montalban J., Noels A., eds, Red Giants as Probes of the Structure and Evolution of the Milky Way, Vol. 26. Springer-Verlag, Berlin, p. 165
Green G. M. et al., 2015, ApJ, 810, 25
Guedes J., Mayer L., Carollo M., Madau P., 2013, ApJ, 772, 36
Gunn J. E. et al., 2006, AJ, 131, 2332
Hayden M. R. et al., 2015, ApJ, 808, 132
Hayden M. R., Recio-Blanco A., de Laverny P., Mikolaitis S., Worley C. C., 2017, A&A, 608, L1
Hayes C. R. et al., 2018, ApJ, 852, 49
Haywood M., Di Matteo P., Lehnert M. D., Katz D., Gómez A., 2013, A&A, 560, A109
Haywood M., Lehnert M. D., Di Matteo P., Snaith O., Schultheis M., Katz D., Gómez A., 2016, A&A, 589, A66
Helmi A., Babusiaux C., Koppelman H. H., Massari D., Veljanoski J., Brown A. G. A., 2018, Nature, 563, 85
Holtzman J. A. et al., 2015, AJ, 150, 148
Howell S. B. et al., 2014, PASP, 126, 398
Izzard R. G., Preece H., Jofre P., Halabi G. M., Masseron T., Tout C. A., 2018, MNRAS, 473, 2984
Jofré P. et al., 2016, A&A, 595, A60
Jofré P., Heiter U., Buder S., 2017, Bull. Astron. Soc. India, 14, 37
Jofré P., Heiter U., Soubiran C., Tucci M. M., Worley C., Hawkins K., Blanco-Cuaresma S., Rodrigo C., 2018, VizieR Online Data Catalog, 2, III/281
Johnson J. A., APOKASC Collaboration, 2016, Astron. Nachr., 337, 917
Jones B. J. T., Wyse R. F. G., 1983, A&A, 120, 165
Jones E. et al., 2001, SciPy: Open Source Scientific Tools for Python, http://www.scipy.org/
Jönsson H. et al., 2018, AJ, 156, 126
Kawata D., Chiappini C., 2016, Astron. Nachr., 337, 976
Keller S. C. et al., 2007, Publ. Astron. Soc. Aust., 24, 1
Khan S. et al., 2019, A&A, 628, A35
Kippenhahn R., Weigert A., 1990, Stellar Structure and Evolution. Springer-Verlag, Berlin
Kippenhahn R., Weigert A., Weiss A., 2012, Stellar Structure and Evolution. Springer-Verlag, Berlin
Kjeldsen H., Bedding T. R., 1995, A&A, 293, 87
Kordopatis G. et al., 2015, A&A, 582, A122
Kubryk M., Prantzos N., Athanassoula E., 2015, A&A, 580, A126
Kunder A. et al., 2017, AJ, 153, 75
Lund M. N., Handberg R., Davies G. R., Chaplin W. J., Jones C. D., 2015, ApJ, 806, 30
Lund M. N. et al., 2016, PASP, 128, 124204

Mackereth T. J. et al., 2017, MNRAS, 471, 3057

Mackereth J. T. et al., 2019, MNRAS, 482, 3426

Madau P., Dickinson M., 2014, ARA&A, 52, 415

Majewski S. R. et al., 2017, AJ, 154, 94

Martig M. et al., 2015, MNRAS, 451, 2230

Martig M., Minchev I., Ness M., Fouesneau M., Rix H.-W., 2016, ApJ, 831, 139

Mathur S. et al., 2010, A&A, 511, A46

Mathur S., García R. A., Huber D., Regulo C., Stello D., Beck P. G., Houmani K., Salabert D., 2016, ApJ, 827, 50

Matteucci F., 2001, The Chemical Evolution of the Galaxy, Vol. 253. Kluwer Acad. Publishers, Dordrecht

Miglio A., 2012, in Miglio A., Montalban J., Noels A., eds, Red Giants as Probes of the Structure and Evolution of the Milky Way, Vol. 26. Springer-Verlag, Berlin, p. 11

Miglio A. et al., 2009, A&A, 503, L21

Miglio A. et al., 2013, MNRAS, 429, 423

Miglio A. et al., 2016, MNRAS, 461, 760

Miglio A. et al., 2017, Astron. Nachr., 338, 644

Minchev I., 2016, Astron. Nachr., 337, 703

Minchev I., Chiappini C., Martig M., 2013, A&A, 558, A9

Minchev I., Chiappini C., Martig M., 2014, A&A, 572, A92

Minchev I., Martig M., Streich D., Scannapieco C., de Jong R. S., Steinmetz M., 2015, ApJ, 804, L9

Mosser B., Appourchaux T., 2009, A&A, 508, 877

Mosser B., Michel E., Samadi R., Miglio A., Davies G. R., Girardi L., Goupil M. J., 2019, A&A, 622, A76

Nidever D. L. et al., 2015, AJ, 150, 173

Noguchi M., 1998, Nature, 392, 253

Paxton B. et al., 2015, ApJS, 220, 15

Pinsonneault M. H. et al., 2014, ApJS, 215, 19

Pinsonneault M. H., Elsworth Y. P., APOKASC, 2017, Am. Astron. Soc. Meeting Abstr. #229. p. 305.05

Pinsonneault M. et al., 2018, Am. Astron. Soc. Meeting Abstr. #231. p. 450.13

Recio-Blanco A. et al., 2014, A&A, 567, A5

Reddy B. E., Lambert D. L., 2008, MNRAS, 391, 95

Rendle B. M. et al., 2019, MNRAS, 484, 771

Ricker G. R. et al., 2015, J. Astron. Telesc., Instrum., Syst., 1, 014003

Rix H.-W., Bovy J., 2013, A&AR, 21, 61

Robin A. C., Reylé C., Fliri J., Czekaj M., Robert C. P., Martins A. M. M., 2014, A&A, 569, A13

Rodrigues T. S. et al., 2014, MNRAS, 445, 2758

Rodrigues T. S. et al., 2017, MNRAS, 467, 1433

Ruchti G. R. et al., 2011, ApJ, 737, 9

Schofield M. et al., 2019, ApJS, 241, 12

Silva Aguirre V. et al., 2015, MNRAS, 452, 2127

Silva Aguirre V. et al., 2018, MNRAS, 475, 5487

Skrutskie M. F. et al., 2006, AJ, 131, 1163

Snaith O., Haywood M., Di Matteo P., Lehnert M. D., Combes F., Katz D., Gómez A., 2015, A&A, 578, A87

Soderblom D. R., 2010, ARA&A, 48, 581

Sommer-Larsen J., Götz M., Portinari L., 2003, ApJ, 596, 47

Steinmetz M., Mueller E., 1994, A&A, 281, L97

Stello D. et al., 2015, ApJ, 809, L3

Stello D. et al., 2017, ApJ, 835, 83

Valentini M. et al., 2016, Astron. Nachr., 337, 970

Valentini M. et al., 2017, A&A, 600, A66

Wolf C. et al., 2018, Publ. Astron. Soc. Aust., 35, e010

Yu J., Huber D., Bedding T. R., Stello D., Hon M., Murphy S. J., Khanna S., 2018, ApJS, 236, 42

Zasowski G. et al., 2017, AJ, 154, 198

[1]*School of Physics and Astronomy, University of Birmingham, Edgbaston Park Rd, Birmingham B15 2TT, UK*

[2]*Stellar Astrophysics Centre, Department of Physics and Astronomy, Aarhus University, Ny Munkegade 120, DK-8000 Aarhus C, Denmark*

[3]*Leibniz-Institut für Astrophysik Potsdam (AIP), An der Sternwarte 16, D-14482 Potsdam, Germany*

[4]*LESIA, Observatoire de Paris, PSL Research University, CNRS, Sorbonne Université, Université Paris Diderot, F-92195 Meudon, France*

[5]*IRFU, CEA, Université Paris-Saclay, F-91191 Gif-sur-Yvette, France*

[6]*AIM, CEA, CNRS, Université Paris-Saclay, Université Paris Diderot, Sorbonne Paris Cité, F-91191 Gif-sur-Yvette, France*

[7]*Instituto de Astrofísica de Canarias, E-38200 La Laguna, Spain*

[8]*Dpto. de Astrofísica, Universidad de La Laguna, E-38205 La Laguna, Tenerife, Spain*

[9]*Space Science Institute, 4750 Walnut Street Suite 205, Boulder, CO 80301, USA*

[10]*Núcleo de Astronomía, Facultad de Ingenier ía y Ciencias, Universidad Diego Portales, Av. Ejército 441, Santiago, Chile*

[11]*Institute of Astronomy, University of Cambridge, Madingley Rise, Cambridge CB3 0HA, UK*

[12]*Research School of Astronomy and Astrophysics, Mount Stromlo Observatory, The Australian National University, ACT 2611, Australia*

[13]*Osservatorio Astronomico di Padova-INAF, Vicolo dell'Osservatorio 5, I-35122 Padova, Italy*

[14]*Max-Planck-Institut für Astronomie, Königstuhl 17, D-69117 Heidelberg, Germany*

[15]*Department of Physics and Astronomy, Uppsala University, Box 516, SE-75120 Uppsala, Sweden*

[16]*INAF-Osservatorio Astrofisico di Arcetri, Largo E. Fermi, 5, I-50125 Firenze, Italy*

[17]*Department of Astronomy, Ohio State University, 140 W 18th Ave, Columbus, OH 43210, USA*

[18]*Center for Cosmology and AstroParticle Physics, 191 West Woodruff Avenue, Ohio State University, Columbus, OH 43210, USA*

[19]*University of Arizona, Tucson, AZ 85719, USA*

[20]*Observatório Nacional, São Cristóvão, Rio de Janeiro 20921-400, Brazil*

[21]*Instituto de Astrofísica, Pontificia Universidad Católica de Chile, Av. Vicuna Mackenna 4860, 782-0436 Macul, Santiago, Chile*

[22]*Millennium Institute of Astrophysics, Av. Vicuña Mackenna 4860, 782-0436 Macul, Santiago, Chile*

[23]*Centro de Astronomía (CITEVA), Universidad de Antofagasta, Avenida Angamos 601, Antofagasta 1270300, Chile*

This paper has been typeset from a TeX/LaTeX file prepared by the author.